Progress In Electromagnetics Research C, Vol. 137, 29–38, 2023

High-Sensitivity Refractive Index Sensor of Arc-Shape Photonic Crystal Fiber Based on Surface Plasmon Resonance

Haiping Li, Juan Ruan*, Xin Li, Qianqian Zhang, Jianjun Chen, Tao He, and Guangyong Wei

Abstract—A surface plasmon resonance-based arc-shaped photonic crystal fiber high-sensitivity refractive index (RI) sensor is proposed. An open arc-shaped analyte channel is produced at the top of the fiber to facilitate RI detection of the analyte, and a gold film is coated inside the arc-shaped structure to stimulate mode coupling. The performance of the sensor is analyzed by using the finite element method (FEM). The results have demonstrated that the sensor can detect a sensing range of 1.35–1.42 with maximum RI sensitivity of 24900 nm/RIU and resolution of 4.01×10^{-6} RIU. Furthermore, the highest figure of merit (FOM) of 661.71 RIU^{-1} is obtained. Additionally, the effects of air hole size and air hole distance on sensitivity are investigated. Finally, the proposed sensor characterizes great potential in biomedical, chemical, and other fields due to its excellent performance.

1. INTRODUCTION

Surface plasmon resonance (SPR) technology is a highly sensitive, real-time monitoring of molecular interactions based on optical principles. Since the SPR effect is highly sensitive and accurate, it is often applied in desalination [1–5], minerals recovery [6, 7], power generation [8], steam generation [9], imaging [10–14], light-to-heat conversion [15–20], fiber-optic sensing [21, 22], and other applications [23–27]. Most commercial SPR sensors are based on prism structures; however, such structures have the disadvantages of bulky structures and costly equipment, restricting the widespread use of SPR sensors [28]. To solve a series of problems caused by the prism structure, Jorgenson and Yee proposed the first SPR-based optic fiber sensor in 1993 [29]. Compared with the traditional SPR sensors, SPR-based fiber optic sensors have the advantages of simple construction, high sensitivity, remote detection, etc., then researchers carry out more and more intensive research on SPR-based optic fiber sensors.

With the intensive research on SPR-based optic fiber sensors, photonic crystal fibers with high birefringence, high degrees of freedom, and excellent transmission characteristics have attracted a lot of attention from researchers. SPR-based photonic crystal fiber sensor is also widely applied in temperature sensing [30, 31], RI sensing [28, 32–34], biological sensing [22], etc. Chen et al. proposed a D-shaped photonic crystal fiber sensor based on surface plasmon resonance with a maximum sensitivity of 11055 nm/RIU in the sensing range of 1.2–1.29 [33]. Yan et al. proposed a V-shaped photonic crystal fiber RI sensor based on surface plasmon resonance with a maximum sensitivity of 18000.5 nm/RIU in the sensing range of 1.47–1.52 [34]. These structures have been proposed to increase the Contact area between the analyte and the sensor and to improve the performance of the sensor. The performance derived from the sensor reveals that the performance of the sensor still needs to be improved. To increase the contact area between the analyte and the sensor and to improve the sensor performance, an arc-shaped photonic crystal fiber sensor based on surface plasmon resonance is proposed in this paper.

Received 14 May 2023, Accepted 17 August 2023, Scheduled 27 August 2023
* Corresponding author: Juan Ruan (ruanj2005@163.com).
The authors are with the School of Electronic and Information Engineering, China West Normal University, Nanchong 637009, China.

In this work, a surface plasmon resonance-based RI sensor for arc-shaped photonic crystal fibers is proposed. The proposed arc structure can increase the contact area between the analyte and the sensor to enhance mode coupling. The proposed tapering diameter structure in photonic crystal fibers is also important for sensor performance enhancement. The research results indicate that the maximum RI sensitivity of the sensor can reach 24900 nm/RIU, and the resolution is 4.01×10^{-6} RIU in the sensing range of 1.35–1.42. The maximum FOM of the sensor is 661.71 RIU^{-1}. The effect of each structure in the sensor on the performance of the sensor was investigated, and the optimal parameters were selected. Finally, the proposed sensor exhibits excellent performance by comparing the sensitivity, FOM, resolution, and sensing range of different sensors

2. SENSOR STRUCTURE AND NUMERICAL MODELING

The cross-section of the proposed arc-shaped photonic crystal fiber (PCF)-SPR sensor is illustrated in Figure 1. The proposed PCF-SPR structure consists of three layers of regularly arranged air holes. The first layer of six air holes with a distance of $r1 = 1.7\,\mu\text{m}$ is arranged in a positive hexagonal shape with a diameter of $d1 = 0.7\,\mu\text{m}$ and the second and third layers of air holes with radius $r2 = 3.6\,\mu\text{m}$ and $r3 = 5.5\,\mu\text{m}$ arranged in a fan shape with a diameter $d2 = 1\,\mu\text{m}$ and $d3 = 1.4\,\mu\text{m}$, respectively. An arc-shaped channel is fabricated at the top of the PCF, located at a distance of $h = 3.5\,\mu\text{m}$ from the center of the PCF structure, and the radius of the fiber core is $r = 6.5\,\mu\text{m}$. To assure the accuracy of the calculation, the outermost layer of the fiber core employs a perfectly matched layer as the absorption boundary condition. The six air holes in the first layer have a very important adjustment function for mode coupling and sensitivity enhancement. The sensor's mode coupling is improved by designing a structure with fewer vertically oriented air holes.

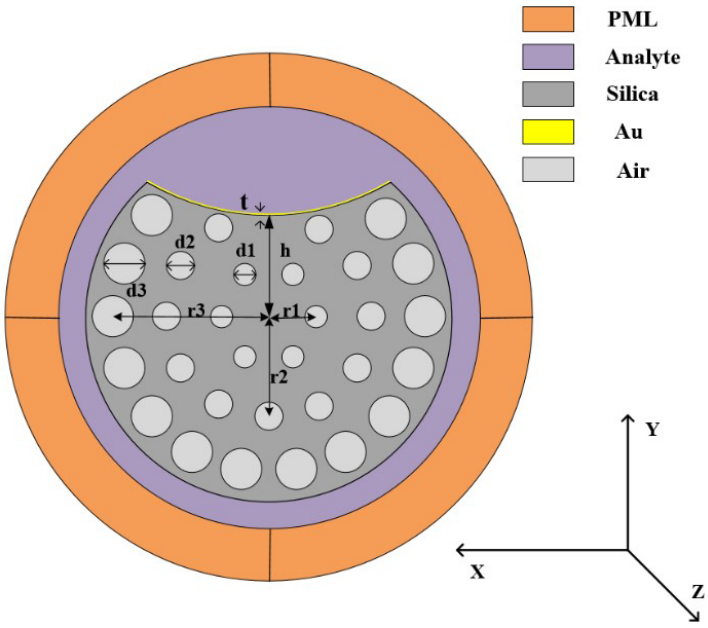

Figure 1. Cross section of the proposed arc-shape structure PCF-SPR sensor.

The background material of the arc-shaped PCF-SPR RI sensor is pure silica, and its RI can be obtained by the Sellmeier equation [35].

$$n^2 - 1 = \frac{0.696166\lambda^2}{\lambda^2 - 0.0684043^2} + \frac{0.4079426\lambda^2}{\lambda^2 - 0.1162414^2} + \frac{0.8974794\lambda^2}{\lambda^2 - 9.896161^2} \tag{1}$$

where λ denotes the wavelength of the incident light and n denotes the RI of silica. The dielectric constant of the gold film coated on the surface of the arc-shaped structure can be obtained by the

Drude-Lorentz model [36].

$$\varepsilon_{Au} = \varepsilon_{\infty} - \frac{\omega_D^2}{\omega(\omega + j\gamma_D)} - \frac{\Delta\varepsilon \cdot \Omega_L^2}{(\omega^2 - \Omega_L^2) + \mathrm{j}\Gamma_L\omega} \tag{2}$$

where ε_{∞} is the high-frequency dielectric constant of gold; ω is the angular frequency of light; ω_D and γ_D are the plasma frequency and damping frequency, respectively; Ω_L and Γ_L are the frequency and spectral width of Lorentz oscillator, respectively; $\Delta\varepsilon$ is the weight factor. The confinement loss of different analytes can be calculated by the following equation [36].

$$\alpha = 8.686 \times \frac{2\pi}{\lambda} \times \mathrm{Im}(n_{eff}) \times 10^4 \,(\mathrm{dB/cm}) \tag{3}$$

where $\mathrm{Im}(n_{eff})$ denotes the imaginary part of the effective RI. The sensitivity and FOM of the sensor can be expressed by Equations (4) and (5) [37].

$$S\,(\mathrm{nm/RIU}) = \frac{\Delta\lambda_{\mathrm{peak}}}{\Delta n_a} \tag{4}$$

$$\mathrm{FOM}\,(\mathrm{RIU}^{-1}) = \frac{S}{\mathrm{FWHM}} \tag{5}$$

where FWHM denotes the full width at half-maximum of loss spectra. The performance of the sensor is also evaluated by the wavelength resolution [38].

$$R = \frac{\Delta n_a \cdot \Delta\lambda_{\mathrm{min}}}{\Delta\lambda_{\mathrm{peak}}} \tag{6}$$

where $\Delta\lambda_{\mathrm{min}}$ is the minimum spectral resolution set as 0.1 nm.

3. PERFORMANCE ANALYSIS AND STRUCTURE OPTIMIZATION

SPR occurs when the core mode of the PCF-SPR RI sensor and the surface plasmon polarization (SPP) mode couple at a specific wavelength, and the evanescent field excitation of the metal-free electrons of the incident light couples the energy from the core mode to the SPP mode [39]. The proposed structure is asymmetric, which also leads to an enhanced birefringence effect in the PCF sensor so that the confined field in the PCF has two fundamental modes in the orthogonal axis (X- and Y-polarization core mode) [32]. Figure 2 illustrates the confinement loss spectra of the core mode in the Y (black line)

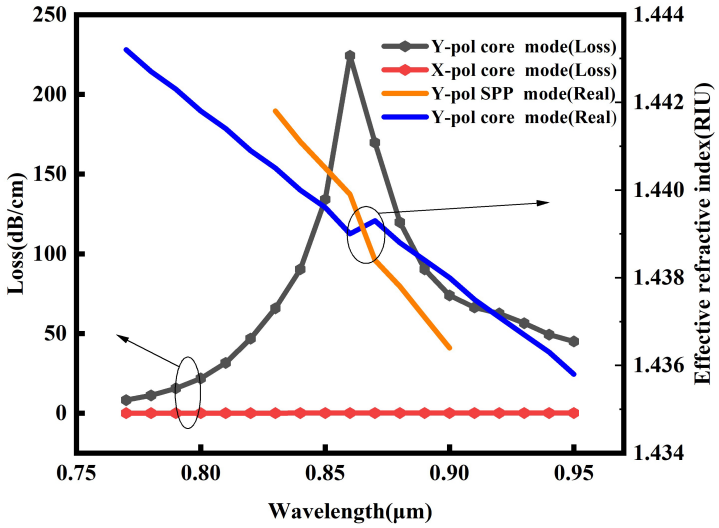

Figure 2. Confinement loss spectra and dispersion relations for sensor core mode and SPP mode at RI $n = 1.41$.

and X polarization (X-pol) (red line) directions and the dispersion curves of the SPP mode and core mode in the Y-pol direction for an analyte RI of $n = 1.41$. It can be concluded that the resonance intensity in the Y-pol direction is much stronger than that in the X-pol direction, and a loss peak is formed at $\lambda = 0.862\,\mu m$. Therefore, the Y-pol direction is chosen to investigate the sensor performance in the following investigation. At the resonant wavelength $\lambda = 0.862\,\mu m$, the effective refractive indexes of the SPP mode in the Y-pol direction and the core mode in the Y-pol direction are equal in the real part, and this intersection point is called the phase matching point, and the loss of the Y-pol core mode reaches the maximum at this point.

Figure 3 illustrates the electric field distribution in the Y-pol direction at wavelength $\lambda = 0.8\,\mu m$, $\lambda = 0.862\,\mu m$, and $\lambda = 0.9\,\mu m$, and the electric field distribution in the X-pol direction at wavelength $\lambda = 0.862\,\mu m$. It can be noted that only little energy couples from the core mode to the SPP mode in the Y-pol core mode at $\lambda = 0.8\,\mu m$, and a large amount of energy is still constrained to the core mode. The coupling level in the Y-pol direction is much larger than that of X-pol at $\lambda = 0.862\,\mu m$ as the wavelength increases, and the Y-pol core mode couples the most energy to the Y-pol core mode at this wavelength. Finally, the energy of the SPP mode in the Y-pol direction at wavelength $\lambda = 0.9\,\mu m$ is gradually coupled to the Y-pol core mode as the wavelength increases.

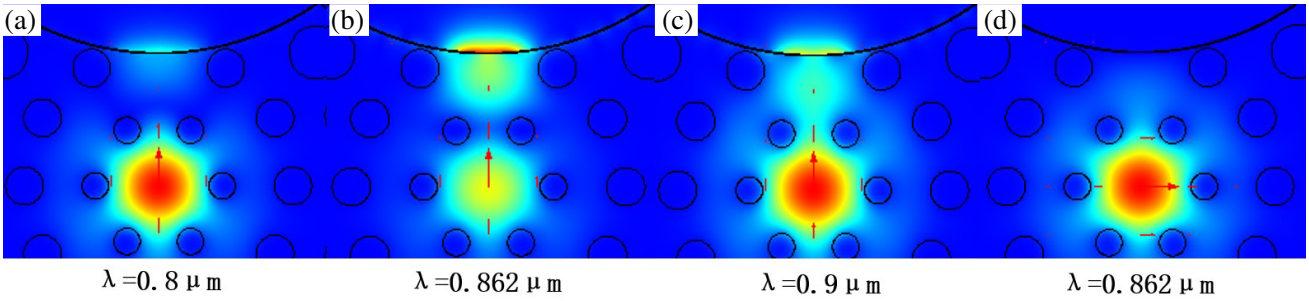

Figure 3. The electric field distribution of the (a), (b), and (c) Y-pol core mode, (d) X-pol core mode at $n = 1.41$.

Changes in sensor structure lead to changes in sensor performance; therefore, sensor performance is improved by optimizing the structure of the sensor. To ensure consistency, other parameters were kept constant, and only one experimental parameter was changed in the subsequent simulation experiments. The subsequent optimization process for the sensitivity calculation uses refractive indexes of $n = 1.41$ and $n = 1.42$.

As shown in Figure 4(a), the loss spectrum has a redshift with the increase of the air hole size $d1$, and the loss peak is almost unchanged. This phenomenon is caused by the increase of the air hole diameter $d1$, which decreases the mode field area of the core mode, resulting in a change of the phase matching point and a redshift of the loss spectrum. Figure 4(b) illustrates the influence of different parameters $d1$ on the sensitivity, and it can be concluded that the size of $d1$ has a great influence on the sensitivity of the sensor. Finally, considering the FWHM of the loss spectrum and sensitivity, the optimal value is $d1 = 0.7\,\mu m$.

Figure 5(a) indicates that the loss spectrum has a blueshift, and the peak loss decreases as $r1$ increases. When $r1 = 1.6\,\mu m$, the loss spectrum forms two loss peaks. This is attributed to the fact that the size of $r1$ directly affects the mode field area of the core mode, and the variation of $r1$ also affects the mode coupling between the core mode and the SPP mode. Therefore, the size of $r1$ plays a very important role in adjusting the mode coupling of the sensor. Figure 5(b) illustrates the effect of the change in $r1$ on the sensitivity. It can be observed that the size of $r1$ has a very big impact on the sensitivity. After comprehensive consideration of the size of $r1$ on the FWHM of the loss spectrum and the impact of sensitivity, $r1 = 1.7\,\mu m$ is the optimal value.

Figure 6(a) illustrates the influence of the variation of h on the loss spectrum. It can be noted from the figure that the peak loss decreases, and the FWHM increases with the increase of h. The major reason for this phenomenon is that the increase of h increases the distance between the core mode and

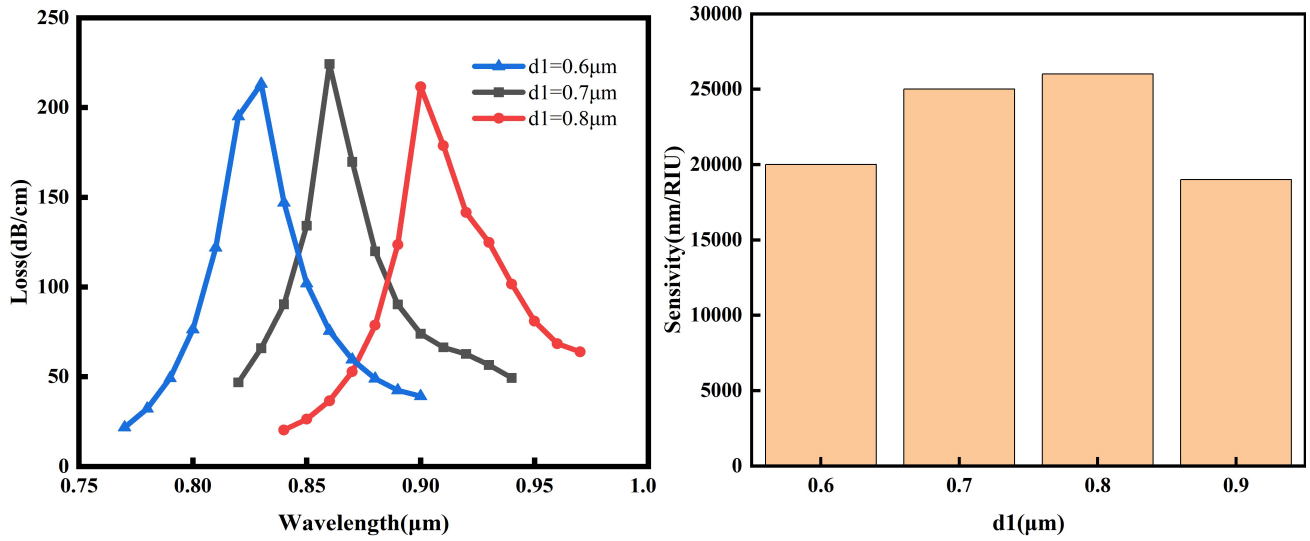

(a) (b)

Figure 4. (a) Loss spectrum and (b) sensitivity under different parameters of $d1$.

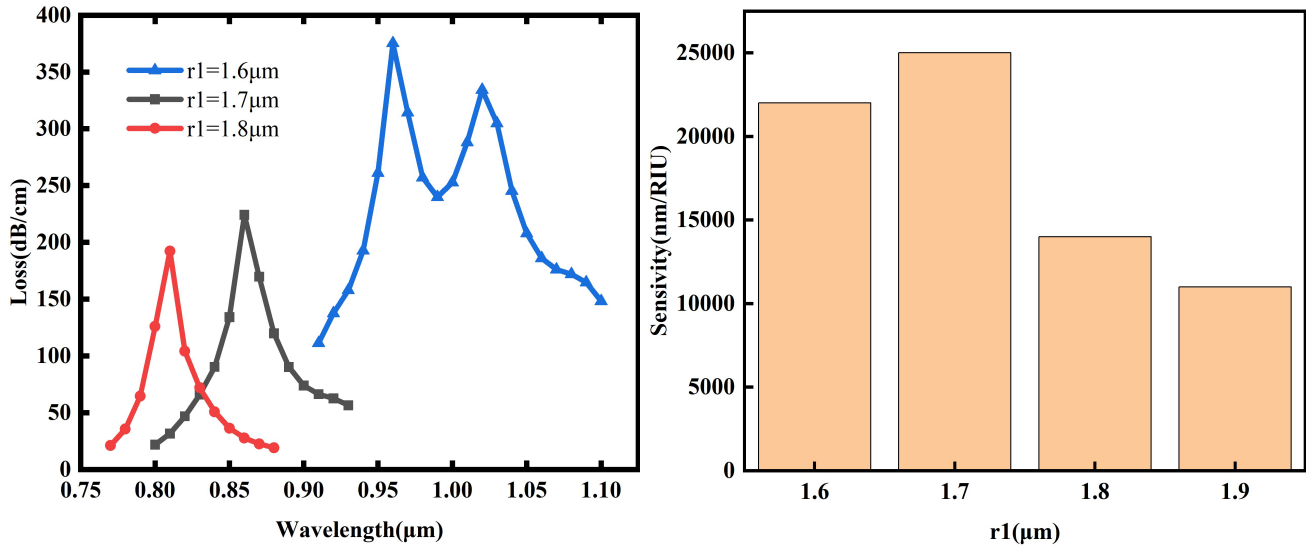

(a) (b)

Figure 5. (a) Loss spectrum and (b) sensitivity under different parameters of $r1$.

the surface of the gold film, resulting in the reduction of the loss of the core mode. Figure 6(b) illustrates the effect of the size of h on the sensitivity of the sensor. The optimal value of h is 3.5 μm based on the comprehensive consideration of FWHM and sensitivity.

Figure 7 illustrates the variation of RI sensitivity with RI at gold film thickness $t_{Au} = 28$ nm, $t_{Au} = 30$ nm, and $t_{Au} = 32$ nm. The corresponding sensitivity is 24900 nm/RIU, 22000 nm/RIU, and 18000 nm/RIU respectively. Therefore, the optimal value is $t_{Au} = 28$ nm after a comprehensive comparison. Finally, the optimal parameters obtained are $d1 = 0.7$ μm, $r1 = 1.7$ μm, $h = 3.5$ μm, and $t_{Au} = 28$ nm.

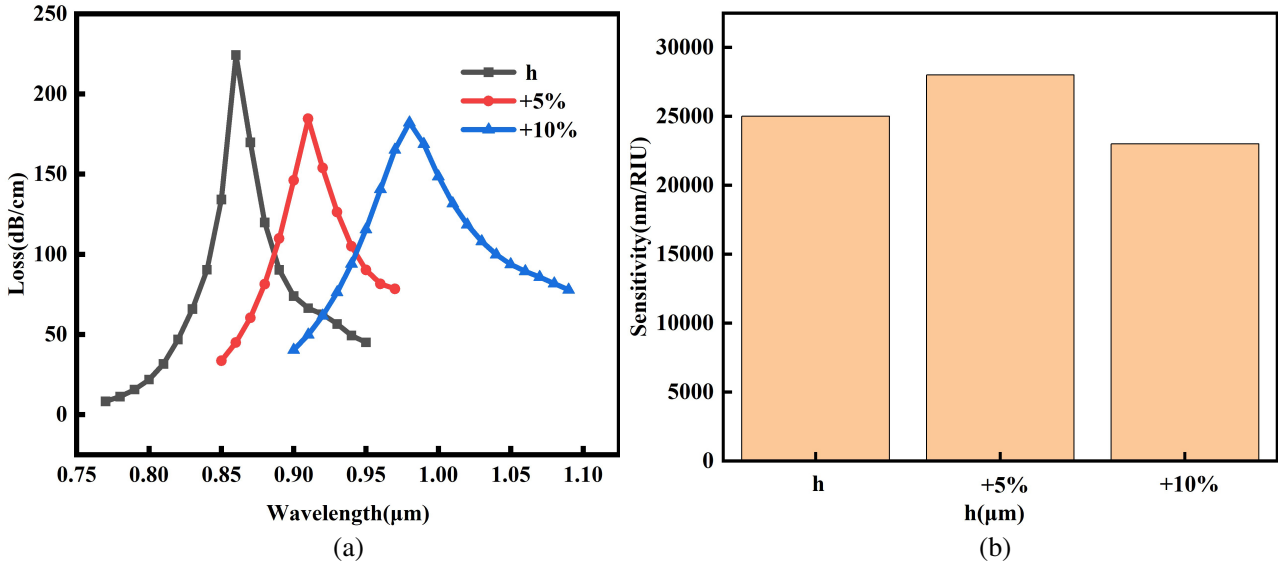

Figure 6. (a) Loss spectrum and (b) sensitivity under different parameters of h.

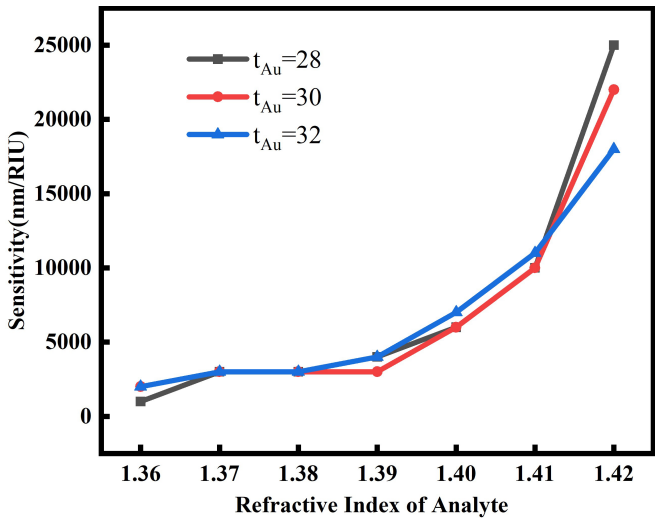

Figure 7. The influence of gold film thickness t_{Au} on sensor sensitivity.

4. ANALYSIS OF THE OPTIMIZED RESULTS

Figure 8(a) depicts the Y-pol core mode loss spectrum in the RI range of 1.35–1.42. It can be observed that the loss spectrum has a redshift, and the loss peak increases as the RI increases. This phenomenon is attributed to the increase of RI causing a redshift of the phase matching point, resulting in a redshift of the loss spectrum. Figure 8(b) depicts the polynomial fit to the resonant wavelength at different refractive indices. The polynomial fitting coefficient is 0.98909.

The calculation of the performance of the RI sensor can be obtained from Table 1. According to the calculation, the maximum sensitivity of the sensor is 24900 nm/RIU; the corresponding resolution is 4.01×10^{-6} RIU; and the maximum FOM is 661.71 RIU^{-1}.

The performance of the sensors compared to different structures is presented in Table 2. The proposed sensor exhibits very excellent performance by comparing the performance of sensors with different structures.

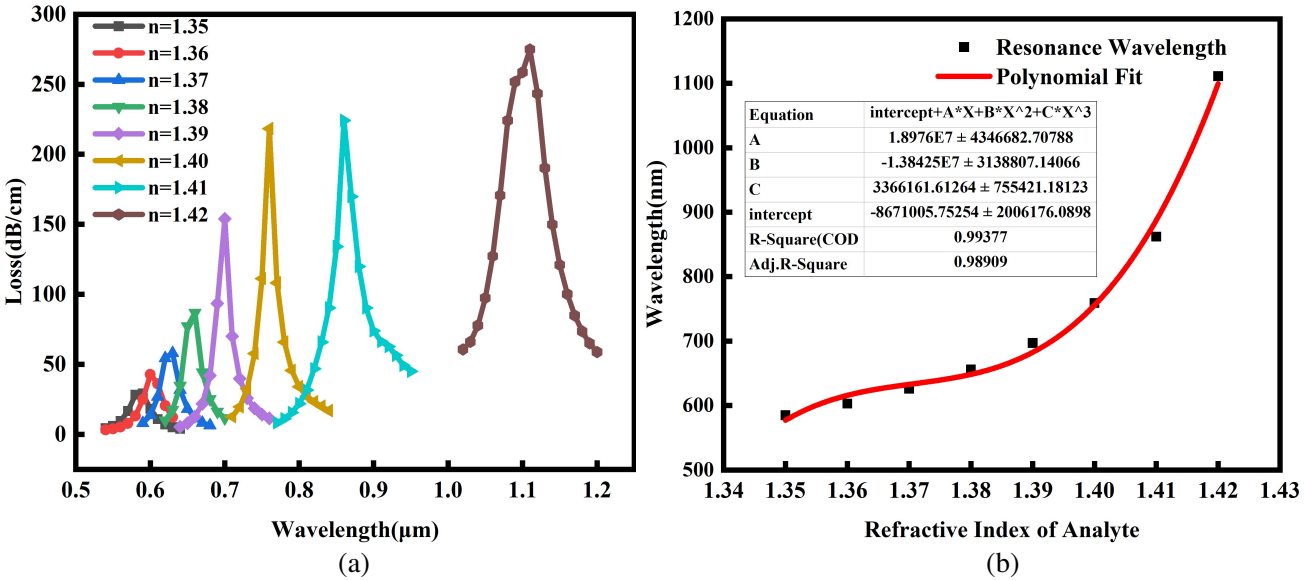

Figure 8. (a) Loss spectrum in Y-pol core mode in the RI range of 1.35–1.42. (b) Polynomial fitting curve of resonant wavelength with RI.

Table 1. Sensor performance for analyte RI of 1.35–1.42.

RI	λ_{peak} (nm)	Loss Peak (dB/cm)	Sensitivity (nm/RIU)	Resolution (RIU)	FWHM (nm)	FOM (RIU^{-1})
1.35	585	31	1800	5.55×10^{-5}	37.88	47.51
1.36	603	44	2300	4.34×10^{-5}	32.41	70.97
1.37	626	65	3000	3.33×10^{-5}	31.34	95.72
1.38	656	101	4100	2.43×10^{-5}	28.41	144.32
1.39	697	194	6200	1.61×10^{-5}	22.39	276.91
1.4	759	218	10300	9.7×10^{-6}	20.28	507.89
1.41	862	224	24900	4.01×10^{-6}	37.63	661.71
1.42	1111	275	/	/	/	/

Table 2. Comparison of the performance of various structural sensors.

Structure	RI range	Max sensitivity (nm/RIU)	Resolution (RIU)	FOM (RIU^{-1})	Ref.
D-shaped PCF	1.2–1.29	11055	/	/	[33]
V-shaped PCF	1.47–1.52	18000.5	/	/	[34]
D-shaped PCF	1.26–1.38	5626.86	1.78×10^{-5}	/	[40]
D-shaped PCF	1.23–1.36	18000	5.56×10^{-6}	/	[41]
TC-NCF	1.16–1.43	12400	8.06×10^{-6}	/	[42]
Arc-shaped PCF	1.35–1.42	24900	4.01×10^{-6}	661.71	This work

5. CONCLUSION

In summary, an arc-shaped photonic crystal fiber RI sensor based on surface plasmon resonance is proposed. The performance of the sensor was investigated by the FEM in COMSOL software. The optimal parameters of the sensor were obtained. According to the calculation, the maximum sensitivity of the sensor is 24900 nm/RIU; the corresponding resolution is 4.01×10^{-6} RIU; and the maximum FOM is 661.71 RIU^{-1}. The proposed arc structure increases the contact area between the analyte and the sensor, and the sensor performance is improved by using an optimized tapering air hole structure. Finally, RI sensors have a wide range of applications, and the proposed sensors have great potential in medical application, environmental monitoring, and other fields owing to its excellent performance.

DATA AVAILABILITY STATEMENT

The resulting data given in this paper are not currently publicly available but can be obtained from the authors upon reasonable request.

CONFLICTS OF INTEREST

The authors declare no conflicts of interest.

ACKNOWLEDGMENT

This work was supported by the Fundamental Research Funds of China West Normal University, China (Grant No. 412881).

REFERENCES

1. Santoro, S., A. H. Avci, A. Politano, and E. Curcio, "The advent of thermoplasmonic membrane distillation," *Chemical Society Reviews*, Vol. 51, 6087–6125, 2022.
2. Abramovich, S., D. Dutta, C. Rizza, S. Santoro, M. Aquino, A. Cupolillo, J. Occhiuzzi, M. F. L. Russa, B. Ghosh, D. Farias, A. Locatelli, D. W. Boukhvalov, A. Agarwal, E. Curcio, M. B. Sadan, and A. Politano, "NiSe and CoSe topological nodal-line semimetals: A sustainable platform for efficient thermoplasmonics and solar-driven photothermal membrane distillation," *Small*, Vol. 18, No. 31, 2201473, 2022.
3. Elmaghraoui, D., A. Politano, and S. Jaziri, "Photothermal response of plasmonic nanofillers for membrane distillation," *The Journal of Chemical Physics*, Vol. 152, 114102, 2020.
4. Politano, A., G. D. Profio, E. Fontananova, V. Sanna, A. Cupolillo, and E. Curcio, "Overcoming temperature polarization in membrane distillation by thermoplasmonic effects activated by Ag nanofillers in polymeric membranes," *Desalination*, Vol. 451, No. 1, 192–199, 2019.
5. Politano, A., P. Argurio, G. D. Profio, V. Sanna, A. Cupolillo, S. Chakraborty, H. A. Arafat, and E. Curcio, "Photothermal membrane distillation for seawater desalination," *Advanced Materials*, Vol. 29, No. 2, 1603504, 2016.
6. Santoro, S., M. Aquino, C. Rizza, J. Occhiuzzi, D. Mastrippolito, G. D'Olimpio, A. H. Avci, J. D. Santis, V. Paolucci, L. Ottaviano, L. Lozzi, A. Ronen, M. Bar-Sadan, D. S. Han, A. Politano, and E. Curcio, "Lithium recovery through WS2 nanofillers-promoted solar photothermal membrane crystallization of LiCl," *Desalination*, Vol. 546, No. 15, 116186, 2023.
7. Santoro, S., M. Aquino, C. Rizza, A. Cupolillo, D. W. Boukhvalov, G. D'Olimpio, S. Abramovich, A. Agarwal, M. B. Sadan, A. Politano, and E. Curcio, "Plasmonic nanofillers-enabled solar membrane crystallization for mineral recovery," *Desalination*, Vol. 563, No. 1, 116730, 2023.
8. Avci, A. H., S. Santoro, A. Politano, M. Propato, M. Micieli, M. Aquino, W. J. Zhang, and E. Curcio, "Photothermal sweeping gas membrane distillation and reverse electrodialysis for light-to-heat-to-power conversion," *Chemical Engineering and Processing — Process Intensification*, Vol. 164, 108382, 2021.

9. Politano, A., A. Cupolillo, G. D. Profio, H. A. Arafat, G. Chiarello, and E. Curcio, "When plasmonics meets membrane technology," *Journal of Physics: Condensed Matter*, Vol. 28, 363003, 2016.
10. Viti, L., J. Hu, D. Coquillat, A. Politano, W. Knap, and M. S. Vitiello, "Efficient terahertz detection in black-phosphorus nano-transistors with selective and controllable plasma-wave," *Scientific Reports*, Vol. 6, 20474, 2016.
11. Viti, L., D. Coquillat, A. Politano, K. A. Kokh, Z. S. Aliev, M. B. Babanly, O. E. Tereshchenko, W. Knap, E. V. Chulkov, and M. S. Vitiello, "Plasma-wave terahertz detection mediated by topological insulators surface states," *Nano Letters*, Vol. 16, 80–87, 2016.
12. Agarwal, A., M. S. Vitiello, L. Viti, A. Cupolillo, and A. Politano, "Plasmonics with two-dimensional semiconductors: From basic research to technological applications," *Nanoscale*, Vol. 10, No. 19, 8938–8946, 2018.
13. Politano, A., L. Viti, and M. S. Vitiello, "Optoelectronic devices, plasmonics and photonics with topological insulators," *APL Mater*, Vol. 5, 035504, 2017.
14. Pogna, E. A. A., L. Viti, A. Politano, M. Brambilla, G. Scamarcio, and M. S. Vitiello, "Mapping propagation of collective modes in Bi_2Se_3 and $Bi_2Te_{2.2}Se_{0.8}$ topological insulators by near-field terahertz nanoscopy," *Nature Communications*, Vol. 12, 6672, 2021.
15. Politano, A., V. Formoso, and G. Chiarello, "Annealing effects on the plasmonic excitations of metal/metal interfaces," *Applied Surface Science*, Vol. 255, No. 11, 6038–6042, 2009.
16. Politano, A., "Interplay of structural and temperature effects on plasmonic excitations at noble-metal interfaces," *Philosophical Magazine*, Vol. 92, No. 6, 2012.
17. Qiu, G. Y., Z. B. Gai, L. Saleh, J. K. Tang, T. Gui, G. A. K. Kullak-Ublic, and J. Wang, "Thermoplasmonic-assisted cyclic cleavage amplification for self-validating plasmonic detection of SARS-CoV-2," *ACS Nano*, Vol. 15, 7536, 2021.
18. Kang, H. K., W. Hong, Y. J. An, S. Yoo, H. J. Kwon, and Y. Nam, "Thermoplasmonic optical fiber for localized neural stimulation," *ACS Nano*, Vol. 14, 11406, 2020.
19. Herzog, J. B., M. W. Knight, and D. Natelson, "Thermoplasmonics: Quantifying plasmonic heating in single nanowires," *Nano Letters*, Vol. 14, 499, 2020.
20. Baffou, G., R. Quidant, and C. Girard, "Thermoplasmonics modeling: A Green's function approach," *Physical Review B*, Vol. 82, 165424, 2010.
21. Lee, J. H., B. C. Kim, B. K. Oh, and J. W. Choi, "Highly sensitive localized surface plasmon resonance immunosensor for label-free detection of HIV-1," *Nanomedicine: Nanotechnology, Biology and Medicine*, Vol. 9, No. 7, 1018–1026, 2013.
22. Rifat, A. A., R. Hasan, R. Ahmed, and H. Butt, "Photonic crystal fiber-based plasmonic biosensor with external sensing approach," *Journal of Nanophotonics*, Vol. 12, No. 1, 012503, 2018.
23. Maier, S. A., *Plasmonics: Fundamentals and Applications*, 1st Edition, Springer, New York, 2007.
24. Ozbay, E., "Plasmonics: Merging photonics and electronics at nanoscale dimensions," *Science*, Vol. 311, 189, 2006.
25. Hayashi, S. and T. Okamoto, "Plasmonics: Visit the past to know the future," *Journal of Physics D: Applied Physics*, Vol. 45, 10927, 2014.
26. Politano, A. and G. Chiarello, "Plasmon modes in graphene: Status and prospect," *Nanoscale*, Vol. 6, 10927, 2014.
27. Politano, A., G. Chiarello, and C. Spinella, "Plasmon spectroscopy of graphene and other two-dimensional materials with transmission electron microscopy," *Materials Science in Semiconductor Processing*, Vol. 65, 88, 2017.
28. Han, H. X., D. L. Hou, L. Zhao, N. N. Luan, L. Song, Z. H. Liu, Y. D. Lian, J. F. Liu, and Y. S. Hu, "Large detection-range plasmonic sensor based on an H-shaped photonic crystal fiber," *Sensors*, Vol. 20, No. 4, 1009, 2020.
29. Jorgenson, R. C. and S. S. Yee, "A fiber-optic chemical sensor based on surface plasmon resonance," *Sensors and Actuators B: Chemical*, Vol. 12, No. 3, 213–220, 1993.

30. Li, H. P., J. Ruan, X. Li, G. Y. Wei, and T. He, "High-sensitivity temperature sensor based on surface plasmon resonance photonic crystal fiber," *Progress In Electromagnetics Research M*, Vol. 116, 11–21, 2023.
31. Mei, C., Y. Wu, S. Qiu, J. H. Yuan, X. Zhou, and K. P. Long, "Design of dual-core photonic crystal fiber for temperature sensor based on surface plasmon resonance effect," *Optics Communications*, Vol. 508, 127838, 2022.
32. Ahmed, T., F. Haider, R. A. Aoni, and R. Ahmed, "Highly sensitive U-shaped micro-channel photonic crystal fiber-based plasmonic biosensor," *Plasmonics*, Vol. 16, No. 6, 2215–2223, 2021.
33. Chen, X., L. Xia, and C. Li, "Surface plasmon resonance sensor based on a novel D-shaped photonic crystal fiber for low refractive index detection," *IEEE Photonics Journal*, Vol. 10, No. 1, 1–9, 2018.
34. Yan, X., R. Fu, T. L. Cheng, and S. G. Li, "A highly sensitive refractive index sensor based on a V-shaped photonic crystal fiber with a high refractive index range," *Sensors*, Vol. 21, No. 11, 3782, 2021.
35. Yang, H., M. Wang, G. Y. Wang, and J. Q. Yao, "Highly sensitive refractive index sensor based on SPR with silver and titanium dioxide coating," *Optical and Quantum Electronics*, Vol. 53, No. 6, 341, 2021.
36. Zhang, S., J. Li, S. Li, Q. Liu, J. Wu, and Y. Guo, "Surface plasmon resonance sensor based on D-shaped photonic crystal fiber with two micro-openings," *Journal of Physics D: Applied Physics*, Vol. 51, No. 30, 305104, 2018.
37. An, G. W., S. G. Li, X. Yan, X. N. Zhang, Z. Y. Yuan, H. Y. Wang, Y. N. Zhang, X. P. Hao, Y. N. Shao, and Z. C. Han, "Extra-broad photonic crystal fiber refractive index sensor based on surface plasmon resonance," *Plasmonics*, Vol. 12, 465–471, 2017.
38. Yang, Z., L. Xia, C. Li, X. Chen, and D. M. Liu, "A surface plasmon resonance sensor based on concave-shaped photonic crystal fiber for low refractive index detection," *Optics Communications*, Vol. 430, 195–203, 2019.
39. Wang, S. T., Y. H. Lu, W. B. Ma, N. Liu, and S. H. Fan, "D-shaped surface plasmon photonic crystal fiber temperature sensor," *Plasmonics*, Vol. 17, No. 5, 1911–1919, 2022.
40. Pan, H. G., F. Pan, A. L. Zhang, C. B. Cao, and F. J. Xue, "Wide refractive index detection range surface plasmon resonance sensor based on D-shaped photonic crystal fiber," *Optical and Quantum Electronics*, Vol. 54, No. 6, 393, 2022.
41. Zhang, Y., Z. Yi, Y. Shi, C. Liu, X. L. Li, J. W. Lv, L. Yang, and P. K. Chu, "Photonic fibre crystal sensor with a D-shape based on surface plasma resonance containing microfluidic channels for detection of a wide range of refractive indexes," *Journal of Modern Optics*, Vol. 69, No. 1, 1–11, 2022.
42. Zhang, Z. C., J. H. Yuan, S. Qiu, G. Y. Zhou, X. Zhou, B. B. Yan, Q. Wu, K. R. Wang, and X. Z. Sang, "Numerical simulation of a truncated cladding negative curvature fiber sensor based on the surface plasmon resonance effect," *Chinese Physics B*, Vol. 32, 034208, 2023.